Geochemistry, Geophysics, Geosystems

RESEARCH ARTICLE
10.1029/2020GC009143

The Role of Deformation Bands in Dictating Poromechanical Properties of Unconsolidated Sand and Sandstone

Peter K. Miller[1], **Chris Marone**[2], **and Demian M. Saffer**[1]

[1]Institute for Geophysics, University of Texas, Austin, TX, USA, [2]Department of Geoscience and Center for Geomechanics, Geofluids, and Geohazards, The Pennsylvania State University, University Park, PA, USA

Key Points:
- Cataclastic deformation bands affect the hydraulic properties of porous sandstone
- Permeability and seismic velocity decrease in cataclastic deformation bands
- Deformation bands can act as confining structures to fluid reservoirs

Correspondence to:
P. K. Miller,
pkmiller1@utexas.edu

Citation:
Miller, P. K., Marone, C., & Saffer, D. M. (2020). The role of deformation bands in dictating poromechanical properties of unconsolidated sand and sandstone. *Geochemistry, Geophysics, Geosystems*, *21*, e2020GC009143. https://doi.org/10.1029/2020GC009143

Received 27 APR 2020
Accepted 10 SEP 2020
Accepted article online 15 SEP 2020

Abstract Cataclastic shear bands in sands and sandstones are typically stronger, stiffer, and exhibit lower permeability than the surrounding matrix, and therefore act as barriers to fluid flow. Previous work has quantified the reduction in permeability associated with these features; however, little is known about the role of shear band structure in controlling the way they impact permeability and elastic properties. Here, we report on a suite of laboratory measurements designed to measure the poromechanical properties for host material and natural shear bands, over effective stresses from 1–65 MPa. In order to investigate the role of host material properties in controlling poromechanical evolution with stress, we sampled shear bands from two well-studied sandstones representing structurally distinct end-members: a poorly cemented marine terrace sand from the footwall of the McKinleyville thrust fault in Humboldt County, California, and a strongly-cemented sandstone from the hanging wall of the Moab Fault in Moab, Utah. The permeability-porosity trends are similar for all samples, with permeability decreasing systematically with increasing effective stress and decreasing porosity. The permeability of the host material is consistently >1 order of magnitude greater than the shear bands for both localities. For the unconsolidated case, shear bands are less permeable and stiffer than the host material, whereas for the consolidated case, shear bands are slightly less permeable, and wave speeds are slower than in the host. We attribute the differences between the McKinleyville and Moab examples to changes in structure of the nearby host material that accompanied formation of the shear band.

1. Introduction

Cataclastic shear bands can play a significant role in controlling the poromechanical properties of sand-rich sediment and sedimentary rocks. These bands are structurally strong, low-porosity zones that generally form in high-porosity sedimentary rocks in response to strain localization in the upper few kilometers of the Earth's crust (Antonellini et al., 1994; Aydin, 1978; Aydin & Johnson, 1983; K. Cashman & S. Cashman, 2000; Fossen et al., 2007; Fossen & Hesthammer, 1998). Unlike low-porosity rocks in which brittle fractures accommodate deformation, high-porosity rocks deform in localized bands ~1 to 50 mm thick (Aydin, 1978; David et al., 2001; Heap et al., 2015). However, little is known regarding the effect that deformation bands have on the mechanical properties of the host material and how that might impact fluid reservoir properties or porous fault zones.

Shear bands form via deformation that accommodates small displacements, ranging from a few to tens of mm (Aydin, 2000; Fossen, 2010; Perez, 2010). Kinematically, these bands can form as a result of pure shear, simple shear, or a combination of the two (Fossen et al., 2007; Kaproth et al., 2010; Skurtveit et al., 2013). In cataclastic bands, grain size reduction occurs via grain spalling and fracture (Rawling & Goodwin, 2003). The spacing between shear bands and the factors that cause multiple bands to form in close proximity are poorly understood. Previous works show that strain accommodation on individual deformation bands is arrested due to strain hardening, leading to gradual migration of localized deformation and thickening of the bands (Aydin, 1978; Fossen, 2010; Schultz & Siddharthan, 2005).

Localized pore collapse in sandstones during deformation band formation is suggested to compartmentalize hydrocarbon reservoirs by reducing permeability normal to the structures (Aydin, 2000; Rotevatn et al., 2013;

Sample et al., 2006). The band length and orientation with respect to the flow field dictate the magnitude of this effect. Aydin (2000) also recognized the anisotropic nature of deformation bands and accounted for a conduit effect caused by optimally oriented fractures within damage zones.

The formation of deformation bands has been investigated in laboratory experiments (Heap et al., 2015; Kaproth et al., 2010; Skurtveit et al., 2013; Wong et al., 1997). However, studies such as Kaproth et al. (2010) measured properties of deformations created in the laboratory at much higher strains than those observed in the field. Several studies have reported on the permeability and porosity evolution of these features over a range of effective confining pressures (David et al., 2001; Heiland & Raab, 2001; Perez, 2010; Wang & Park, 2002). For example, Wong et al. (2015) documented the transition from brittle failure of porous sandstones by shear localization to cataclastic flow at high confining pressures, at which grain crushing occurs (~200 MPa). They conclude that sandstones become less brittle with increasing porosity and grain size, corresponding to a decrease in the grain crushing pressure (Wong et al., 1997). In addition, Kaproth et al. (2010) showed that the increased abundance of fine particles during deformation band formation results in strain hardening, strengthening the zone relative to the host material. Petrophysical analysis of different deformation band types led Flodin et al. (2003) to conclude that porosity is the controlling parameter for the deformation style and the resulting changes in hydrologic and mechanical properties. Time-dependent deformation (compaction creep) observed in uniaxial and triaxial experiments has also been linked to porosity reduction through intergranular rearrangement and grain cracking (Brzesowsky et al., 2014).

Despite their importance for subsurface fluid flow, there are relatively few detailed laboratory studies of the evolution of hydrologic and mechanical properties of naturally occurring shear bands in the context of changing stress states. In order to understand the effect deformation bands have on the petrophysical properties of the host rock, it is necessary to measure these changes under controlled conditions in the laboratory. Here we report on the differences in permeability and acoustic velocity of host rocks and naturally occurring deformation bands sampled from two end-member sandstones: a compliant, poorly consolidated sand from the McKinleyville thrust fault and a stiff, well-consolidated sand from Moab, Utah. By comparing these two end-members, we aim to investigate the role of the host material state on deformation band characteristics—in both an absolute sense and in terms of the manner and mechanisms by which they modify the host rock properties. In addition, by measuring properties of deformation, which have already formed and undergone some form of diagenesis, we are testing the direct effects of deformation band formation on the host material.

2. Geologic Settings and Background

Shear bands are common features in many sedimentary rocks and are observed in a wide range of sands and sandstones. Our samples differ in their degree of cementation, yet both contain pervasive shear band networks (e.g., Berg & Skar, 2005; Davatzes et al., 2005; Kelsey & Carver, 1988). We collected samples from a poorly cemented marine sand terrace at McKinleyville, CA (Figure 1) and a strongly cemented sandstone from Moab, UT (Figure 1). The selection was designed to sample shear bands formed in host sandstones that exhibit strongly contrasting lithification states.

The McKinleyville fault is one of five imbricate thrust faults that make up the 30 km wide Mad River Fault Zone (MRFZ) in northwestern California. It accommodates ~3.6 km of shortening in response to the northward migration of the Mendocino Triple Junction (MTJ) (Kelsey & Carver, 1988). The McKinleyville fault member of the MRFZ trends northwest to southeast and dips approximately 30°NE, extends 40 km inland, and has slipped at a rate of 0.9 mm/yr for the past 3 Ma (Kelsey & Carver, 1988). The fault cuts an unconsolidated quaternary marine terrace deposit producing the shear bands used for this study.

The terrace sands associated with the McKinleyville thrust include two sets of conjugate cataclastic deformation bands (K. Cashman & S. Cashman, 2000; Kaproth et al., 2010). One set strikes roughly parallel to the main fault at 320° and dips ~20°N (Perez, 2010), whereas the second set strikes ~110° and dips 10°S. The thickness of the bands ranges from 1–8 cm and they occur as anastomosing clusters that contain lenses of apparently undeformed host sand (K. Cashman & S. Cashman, 2000). Based on the recent history of the fault and the exposure thickness, the depth of formation of the bands is constrained to be < ~100 m (~1 to 5 MPa effective vertical stress under hydrostatic pore pressure conditions) (Kaproth et al., 2010).Our second samples come from the Moab Fault of southeastern Utah. The Moab Fault is a 45-km-long normal fault that cuts the Pennsylvanian aged Paradox evaporate basin (Berg & Skar, 2005). The fault accommodates 950 to 1800 m

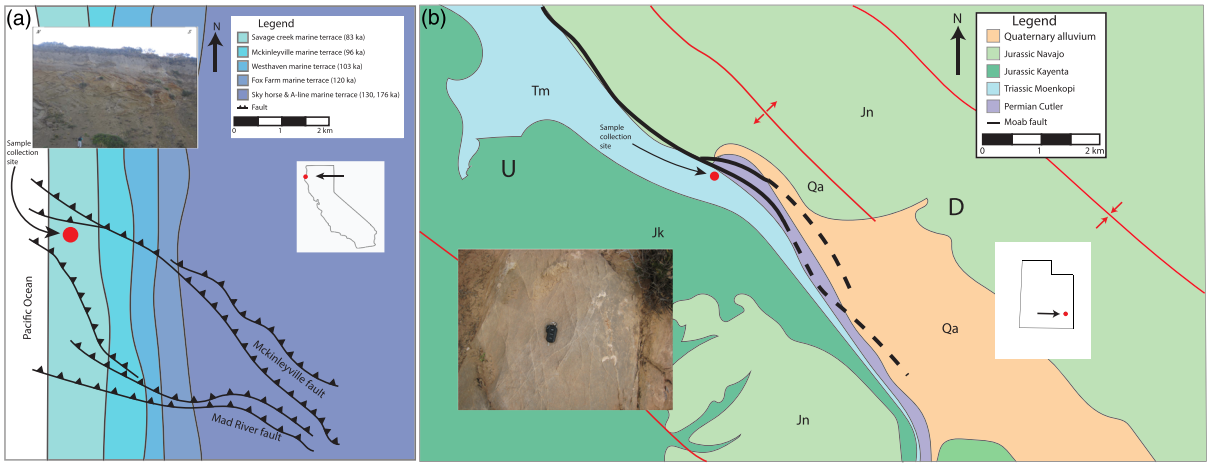

Figure 1. (a) Map showing sampling location within the McKinleyville fault zone (modified from Cashman & Cashman, 2000). Samples for this study were collected from the footwall of the McKinleyville thrust fault (inset image). The fault cuts five poorly consolidated marine terrace formations updip of where it branches from the Mad River fault zone. (b) Map of sampling location within a down-dropped block of the Moenkopi formation (inset image) in the Moab fault zone (modified from Doelling, 2001).

of slip and cuts numerous formations within the basin (Berg & Skar, 2005; Davatzes et al., 2005). Our samples were collected from a down-dropped block of the well-cemented lower Triassic Moenkopi formation (Figure 1). The deformation bands within the Moenkopi formation are 0.5–3 mm thick and accommodate up to 2 mm of displacement. The bands form anastomosing networks that strike subparallel to the Moab Fault. Our sample site was chosen for its proximity to the Moab Fault core and its homogenous units of deformed and undeformed sandstone. Based on the history of the fault and the stratigraphy, the expected depth of formation for these shear bands is 1 to 2.5 km (effective vertical stresses of ~10 to 40 MPa).

3. Methods

To better understand the physical properties of shear bands, their evolution with increasing stress, the differences between types of sand (stones) or between host sands and shear bands, and to illuminate the mechanisms controlling these properties, we conducted experiments to measure permeability, *P* wave velocity, and porosity. Experiments were conducted using a triaxial vessel under hydrostatic stress conditions ($\sigma_1 = \sigma_2 = \sigma_3$) at room temperature and at confining pressures up to 65 MPa (Figure 2). The confining stress (*Pc*) and the axial stress were controlled together, to produce hydrostatic stress, via a single syringe pump. The pressure resolution was 5 kPa and the confining medium was silicon oil. We used distilled water as the pore fluid, and pore pressure (*Pp*) was controlled by syringe pumps connected at each end of the sample, with a pressure resolution of 1 kPa and a volume resolution of 1 mm^3. Axial deformation was recorded by a linear variable differential transformer (LVDT) with a precision of 0.25 μm, and specimen length changes were corrected for apparatus deflection.

We trimmed 25-mm-diameter cylindrical samples containing deformation bands from both localities. These were carefully jacketed, placed between two porous metal frits, and loaded with end caps that contained lead-zirconate-titanate (PZT) piezoelectric transducers (Figure 2**)**. Deformation band samples were 14.5 to 30.0 mm in length. We also conducted tests on the host sand and sandstone. These samples were 25 mm in diameter and 35 to 45 mm in length (Table 1). The McKinleyville specimens comprised isolated deformation bands containing small lenses of host material and were transported from the collection site with great care in order to retain internal structure. However, the total volume of host material is small, such that the specimens consisted almost entirely of deformation band material. In contrast, our Moab samples consisted of thin (0.5–2 mm thick) deformation bands embedded in host material.

Within the testing apparatus, the porous metal frits distribute fluid to the sample faces during saturation and permeability tests. The PZTs located in each endcap produce impulses that propagate through the sample

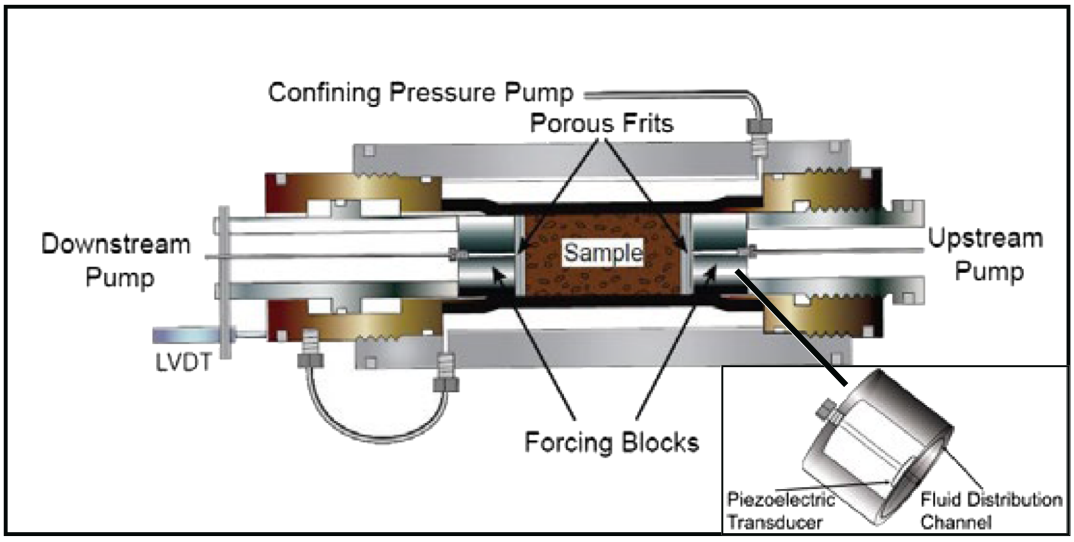

Figure 2. Schematic diagram of triaxial testing system. Inset figure shows the fluid distribution cap with embedded piezoelectric transducer (PZT) (after Carpenter et al., 2014). Deformation is measured using a linearly variable differential transducer (LVDT).

and allow measurement of elastic wave speeds (Figure 2). We follow the notation convention used by Wong et al. (1997), where compressive stresses and compactive strains are defined as positive and dilatant strains are negative.

Once placed in the triaxial vessel, the samples were saturated, confining pressure was applied, and a 100 kPa target pore pressure was achieved at a mean effective confining stress (P_{eff}) of 1 MPa. The temperature of the apparatus was regulated at 29.0 ± 0.1°C to minimize the change in volume of the sample or pore fluid resulting from thermal expansion or contraction. Each sample was step-loaded from 1 to 65 MPa in 5 or 10 MPa increments. At each stress step the permeability, porosity, compressibility, and *P* wave velocity were measured. Volumetric drainage was also monitored to determine when the sample had reached equilibrium at a given applied stress.

Sample deformation was measured by the axial LVDT and by changes in water volume in the upstream and downstream syringe pumps (Figure 2). Axial deformation was measured continuously during each experiment and provides a reliable, high-frequency record of length changes. We focus here on the volumetric strain because it provides a relevant metric for analyzing porosity evolution. The initial increase in P_{eff} at each step produced significant axial and volumetric deformation during primary consolidation (Figure 3)

Table 1
Table of Experiments

Experiment	Material	Sample length (mm)	Sample mass (g)	ρ_b (g/cm^3)	Analyses
T70_347_08B05	Shear band	14.62	12.39	1.67	K, ϕ, V_p, S, G
T70_355_MCKF	Host mat.	42.12	30.23	1.42	K, ϕ, V_p, S, G
T70_359_08B05	Shear band	21.15	18.59	1.73	K, ϕ, V_p
T70_367_08B05	Shear band	33.96	29.39	1.71	K, ϕ, β, V_p
T70_396_MCKF	Host mat.	33.66	25.47	1.49	K, ϕ, β, V_p
T70_397_08B05	Shear band	29.65	26.70	1.77	K, ϕ, β, V_p
T70_399_MBHS	Host mat.	30.60	32.04	2.07	K, ϕ, β, V_p, S, G
T70_408_MCKF	Host mat.	41.00	31.12	1.49	K, ϕ, β, V_p
T70_419_MBDB	Shear band	25.70	22.11	1.69	K, ϕ, β, V_p, S, G
T70_424_MBHS	Host mat.	41.68	42.87	2.02	K, ϕ, β, V_p

Note. The parameters measured at each stress step were permeability (K), porosity (ϕ), *P* wave velocity (V_p), and compressibility (β). The microstructure of each rock type was determined from through grain size analysis (G) and SEM imaging (S).

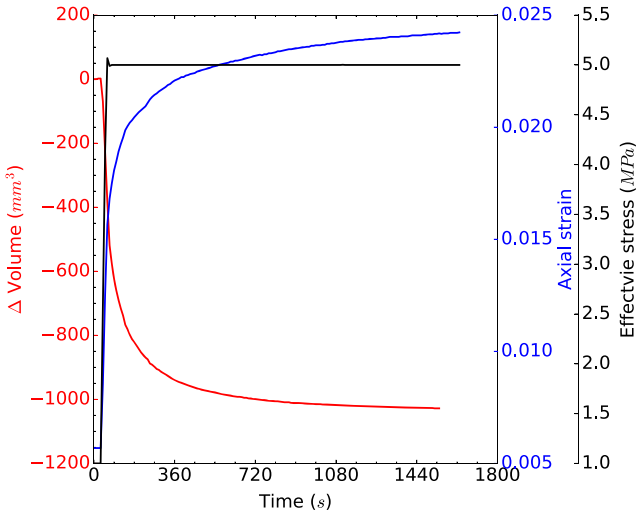

Figure 3. Example of stress step from 1 to 5 MPa, showing confining pressure (black), change in specimen volume (red), and axial strain (blue) as a function of time.

associated with drainage of initial excess pore pressure from loading and followed by time-dependent secondary consolidation, or creep (e.g., Karig & Ask, 2003; Karig & Hou, 1992).

The step loading procedure creates undrained conditions upon initial application of load, which drives drainage and primary consolidation. Therefore, a characteristic drainage time must pass for equilibration of P_f and P_{eff} throughout the test specimen. This drainage time t, scales with the square of the sample length (L) and the inverse of the hydraulic diffusivity (D):

$$t \approx \frac{L^2}{D} \tag{1}$$

For the range of permeability and stiffness of our samples, t is consistently less than a few hundred seconds. For example, Figure 3 shows a record of deformation during primary consolidation, which corresponds to the drainage time. For this particular case—an increase in stress from 1 to 5 MPa, 95% of the volumetric deformation occurred within 300 s after loading.

We compute porosity, static bulk modulus, and compressibility for each sample and track the evolution of these parameters with increasing effective stress. First, the porosity of the specimens was determined at each effective stress by tracking the total volume change at the end of primary consolidation, as measured by the pore fluid pumps (Figure 3). The initial porosity is given by

$$\phi = 1 - \left(\frac{\rho_b}{\rho_s}\right) \tag{2}$$

where ϕ is the porosity, ρ_b is the dry bulk density, and ρ_s is the grain density. The grain density for the shear bands and host sandstone, composed dominantly of quartz, was assumed to be 2.65 g/cm^3. However, unlike the shear bands from McKinleyville, those from Moab comprise a small (<15%) percentage of the total sample volume, and therefore the reported aggregate porosity change as a function of stress for these specimens primarily reflects deformation of the material adjacent to the shear band. The static compressibility is then computed from the volumetric strain associated with each change in stress.

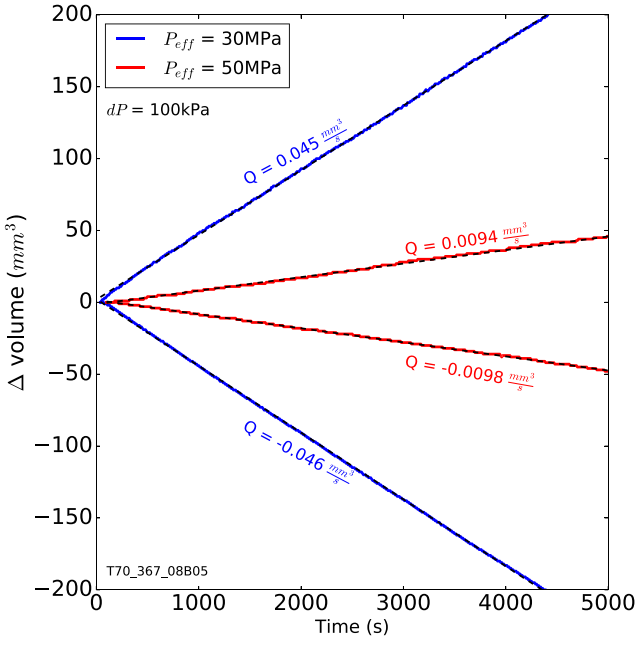

Figure 4. Fluid volumes in the upstream and downstream pumps for two constant head permeability tests, at effective confining pressures of 30 (blue) and 50 MPa (red). Average flow rates (Q) from the two pumps were used to calculate the hydraulic conductivity and permeability of the sample.

The permeability of each sample was measured using a steady state constant head gradient method (Carpenter et al., 2014; Perez, 2010). The measurements were conducted under isostatic loading conditions for P_{eff} ranging from 1 to 65 MPa (in increments of 5 to 10 MPa). For all tests, the maximum values of Pp were <250 kPa, such that the ratio of Pp to Pc remained <10%. As previously noted, the permeability of the deformation band samples was generally measured normal to the band orientation, though one experiment was conducted parallel to band orientation to assess anisotropy. Permeability was measured after equilibration at the end of primary consolidation for each load step.

Permeability measurements were conducted by inducing a fluid pressure gradient across the sample and measuring the resulting volumetric flow rate. The flow rates between the upstream and downstream pumps were allowed to equilibrate (differences of <5% were considered steady state) and then Darcy's law was used to compute the permeability of the sample (Figure 4).

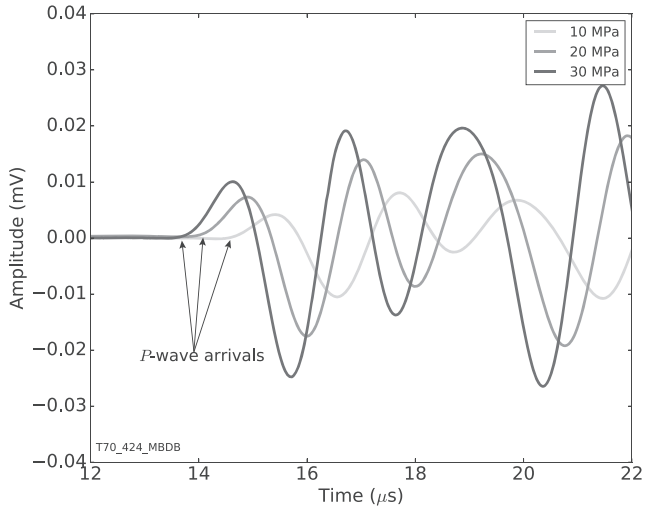

Figure 5. Example waveforms and *P* wave arrival picks from an experiment on Moab deformation bands. The three waveforms were measured at, 10, 20, and 30 MPa mean effective stress, respectively. Note the increase in amplitude and earlier arrival time with increasing stress.

$$\frac{Q}{A} = -K\frac{dh}{dl} \tag{3}$$

$$k = \left(\frac{K\mu}{\rho g}\right) \tag{4}$$

where Q is the flow rate, A is the area perpendicular to flow, dh is the head difference along the length of the sample dl, and K is hydraulic conductivity. In Equation 4, k is the intrinsic permeability, μ is the dynamic viscosity (assumed to be 1.0×10^{-3} Pa s at room temperature conditions), ρ is the fluid density, and g is gravitational acceleration. Due to the high permeability of the samples at low mean effective stress (<10 MPa), a differential pressure between 5 and 10 kPa was used for the constant head tests. Once the sample was brought to effective stresses above 10 MPa the differential pore pressure was raised to 30–100 kPa.

The deformation band samples from McKinleyville were generally thicker than 20 mm and consisted of aggregated bands with small, embedded lenses of host material. The total volume of these lenses was small in proportion to the total sample volume and therefore the permeability reflects that of the shear band material. In contrast, the shear bands within the samples from the Moab Fault are on average 2 mm thick. Unlike the specimens tested from McKinleyville (which were ~100% shear band by volume), the deformation band samples from Moab were <15% shear band by volume. In order to define the permeability of the shear bands themselves, we account for the components of these samples, assuming that flow traverses the shear bands and host material in series (i.e., flow is normal to the shear bands). In this case, the effective permeability of the specimen, as measured in our experiments, is related to the permeability of its constituents by (Fetter, 2001):

$$k_{v\ bulk} = \frac{btot}{\sum_{m=1}^{n}\frac{b_m}{k_{vm}}} \tag{5}$$

Where $k_{v\ bulk}$ is the permeability of the entire specimen, b_{tot} is the total sample thickness including shear bands and surrounding matrix material, b is the layer thickness, and k is the layer permability.

Compressional wave velocities were measured for each sample at each effective stress after the characteristic drainage time had elapsed and the sample reached equilibrium following primary consolidation. For each measurement, pulses were generated by a 500 kHz shear wave PZT in the upstream end cap and recorded via an identical PZT in the downstream cap (Figure 3). The signal was created by 900 V pulses and recorded at 50 MHz (e.g., Carpenter et al., 2014; Hashimoto et al., 2010; Knuth et al., 2013). We stacked 200 waveforms for each record to maximize the signal-to-noise ratio, and picked *P*—arrival times from the raw waveforms. Error in *P* wave arrival picks at low effective stresses is attributed to attenuation and dispersion caused by weak grain contacts. This is observed as a gradual, emergent arrival of the *P* wave, compared to the sharp arrivals at stresses above 10 MPa (Figure 5). Similar attenuation of *P* wave arrivals is observed by Prasad (2002). We define *Vp* by a time-of-flight technique, using measured sample lengths and accounting for travel times through the endcaps and the porous frits using a detailed empirical calibration (Carpenter et al., 2014; Kenigsberg et al., 2020). The *P* wave velocity through the Moab samples represents the velocity of the aggregate sample, including both shear bands and host material.

Particle size distributions (PSD) were measured in a Malvern Mastersizer "S" using the laser diffraction technique detailed in Konert and Vandenberghe (1997), with particular attention to sample handling and analytical procedures (e.g., Storti & Balsamo, 2010). This technique uses the intensity of scattered light from a dispersed sample to determine mean grain size. Grain size data for each sample are reported as a volume percent distribution (Figure 6). Surface images were also taken of the Moab samples using a scanning electron microscope (SEM) and compared to previously acquired images of the McKinleyville samples (Figures 7

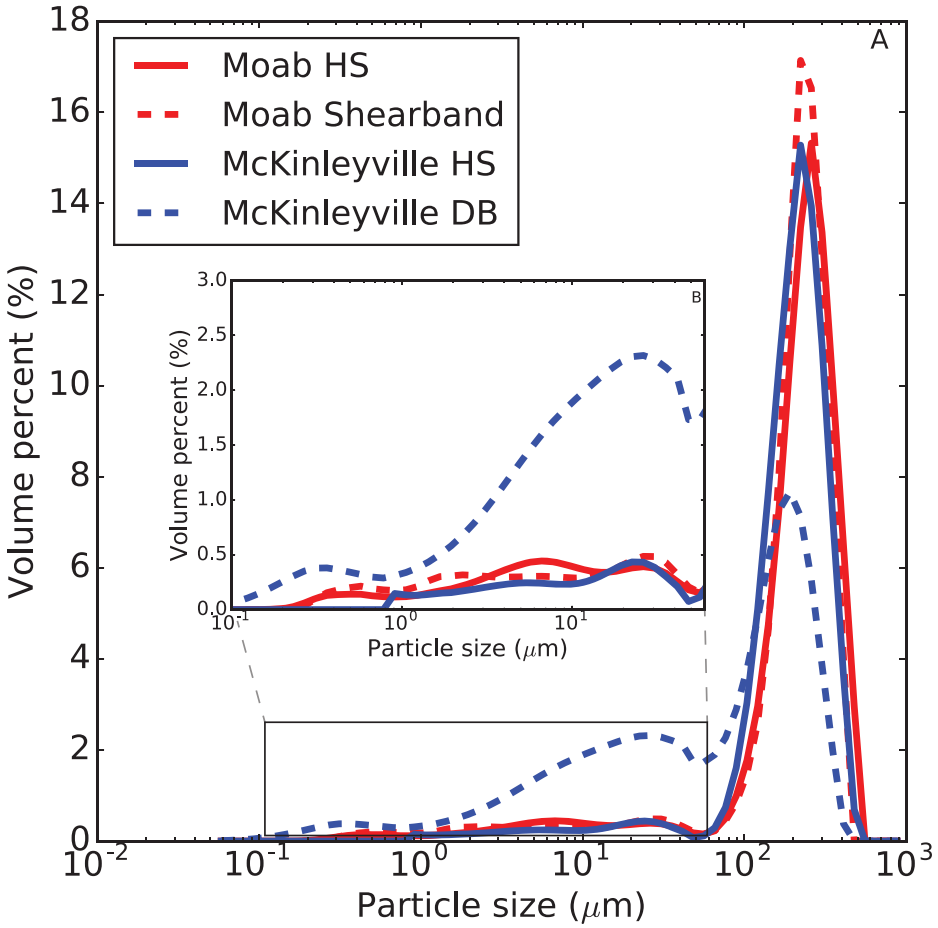

Figure 6. Particle size distribution for samples from McKinleyville and Moab host sands (HS) and deformation bands (DB). The highest volume percent for all samples occurs at a mean grain diameter of 222 μm (panel a). The distribution at smaller grain sizes ranges from 2.5% for 50 μm in the McKinleyville shear band to 0.5% in the McKinleyville host sand and the Moab sandstones (inset panel).

and 8) (Perez, 2010). The SEM provides a qualitative measure of grain size distribution, grain angularity, and the overall microstructure of the material.

4. Results

4.1. Deformation Behavior and Porosity

The deformation behavior of the shear bands is distinctly different than the behavior of the host material. While all of the materials we tested exhibited strain hardening, and two important features are apparent (Figures 9 and 10). First, the McKinleyville host material is generally more compliant than its shear bands, whereas the Moab host sandstone is generally stiffer than material containing shear bands (Figure 10). Second, volumetric strains at peak stress for McKinleyville samples are more variable than for Moab samples. The volumetric strains for the McKinleyville host material range from 0.23 to 0.30 at 65 MPa effective mean stress, while values for the shear bands range from 0.15 to 0.17. A shear band sample from McKinleyville was tested parallel to band orientation (green triangles in Figure 9a) and the results show no significant difference in strain relative to specimens taken perpendicular to the band (blue triangles, Figure 9a). The strains for samples of shear band and host material from Moab at 65 MPa effective mean stress range from 0.035 to 0.055.

Sample porosity decreased as a function of increasing mean effective stress (Figure 9b). The McKinleyville host sand had the highest initial porosities (average 43%) and decreased to 23% as mean effective stress

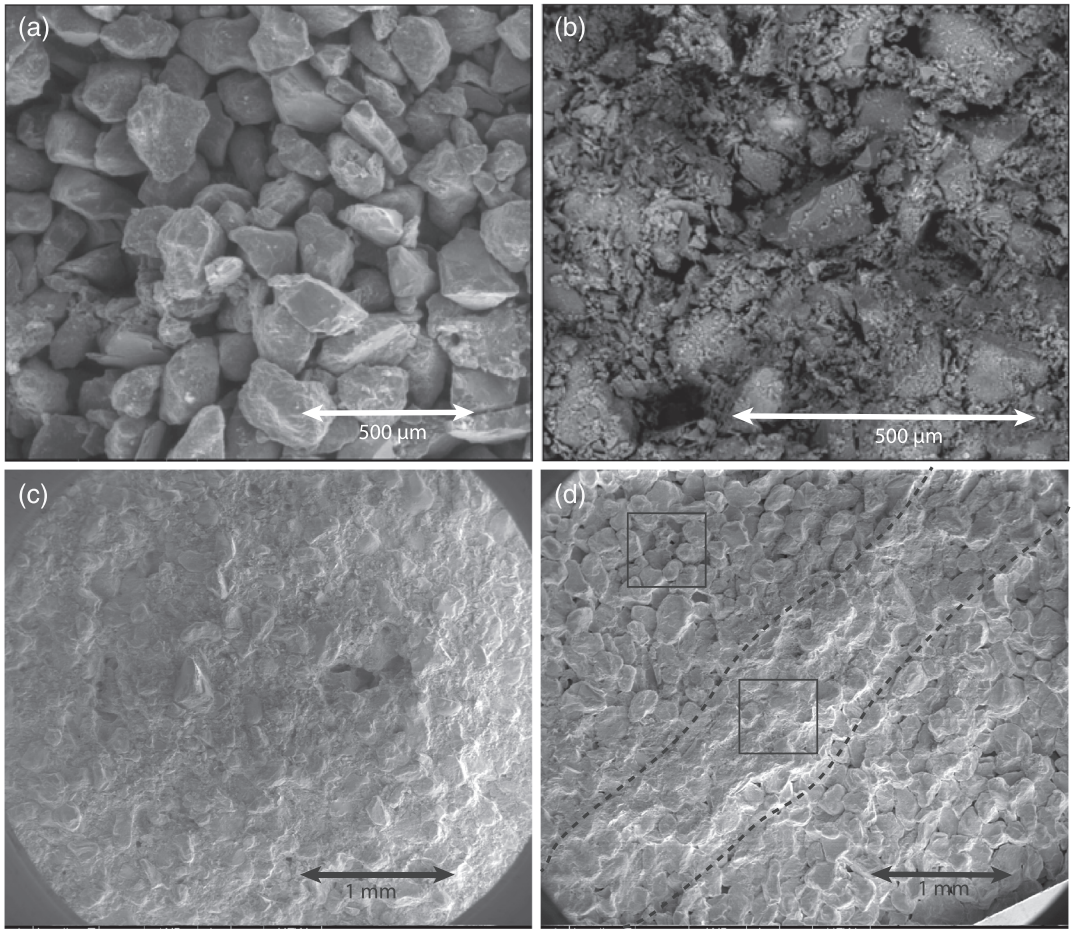

Figure 7. SEM images of the (a) McKinleyville host sand, (b) McKinleyville shear band, (c) Moab host sandstone, and (d) and the Moab shear band. Dashed lines show boundary of ~1-mm-thick shear band, and boxes show locations of images in Figure 8. The scale for the SEM images of the McKinleyville material is 500 μm and the scale for the SEM images of the Moab material is 1 mm.

increased to 65 MPa. The initial porosities of the McKinleyville deformation bands averaged 33% and decreased to 20% at 65 MPa. The Moab samples had initial porosities of 30% (specimens containing shear bands and the host sandstone). Over the stress range from 100 kPa to 65 MPa, the porosity of the shear band material and the host material decreased to 26% and 17%, respectively. However, it should be noted that the Moab shear bands account for a small proportion of the total volume (<10%) of the sample tested, while the shear bands from McKinleyville were isolated and tested essentially independently of the host material.

A clear difference in compliance between the McKinleyville and Moab material is apparent from the slope of the stress–strain curves (Figure 9a). The static bulk modulus was computed for each sample by taking the change in volumetric strain in response to each stress step. The inverse of the bulk modulus, or the compressibilities spanned by the host material and shear bands from McKinleyville at peak stress is 4×10^{-11} Pa^{-1} to 3×10^{-10} (Figure 10). The average difference between host sand and shear band over the effective stress range is half an order of magnitude. In comparison, the compressibility of the Moab material ranges from 6×10^{-11} to 3×10^{-10} near peak stress. Over the stress range, the Moab material is consistently less compliant than the material from McKinleyville (Figure 10).

4.2. Permeability

The permeability-effective stress trends for both the McKinleyville and Moab cases show that the host material is more permeable than the shear bands. Permeability decreases rapidly with increasing effective stress

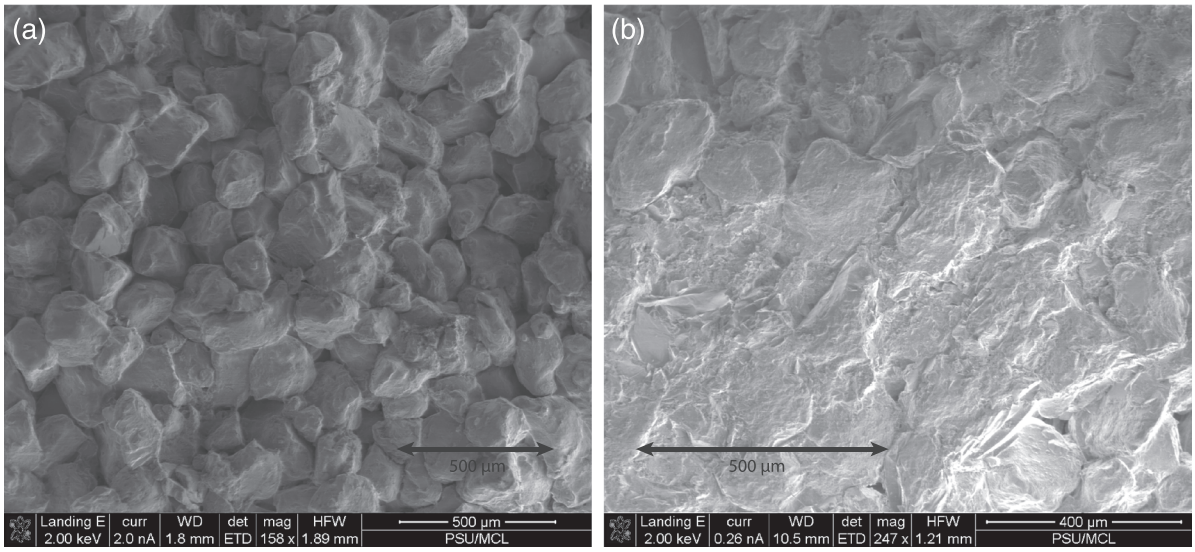

Figure 8. Higher magnification images (500 µm scale) of material adjacent to the deformation band (panel a) and the core of the deformation band (panel b) from the Moab locality. The material adjacent to the shear band is grain supported with a low abundance of cement compared with the shear band core.

up to ~10 MPa. Above 10 MPa, the decrease is more gradual and approximately log-linear (Figure 11), consistent with previous work, for example, David et al. (1994). In our experiments the permeability data for the McKinleyville samples separated into two groups: host sand, which showed a wide range of values at a given stress (>1 order of magnitude; for example, k ranges from 4.0×10^{-16} to 9.0×10^{-15} m^2 at 65 MPa effective stress), and shear bands, which exhibit permeabilities ranging from 2.0×10^{-18} to 1.0×10^{-17} m^2 at peak stress (Figure 11a). Our data are consistent with the trends reported from previous experiments by Perez (2010) on the same McKinleyville host sand and shear band material at effective

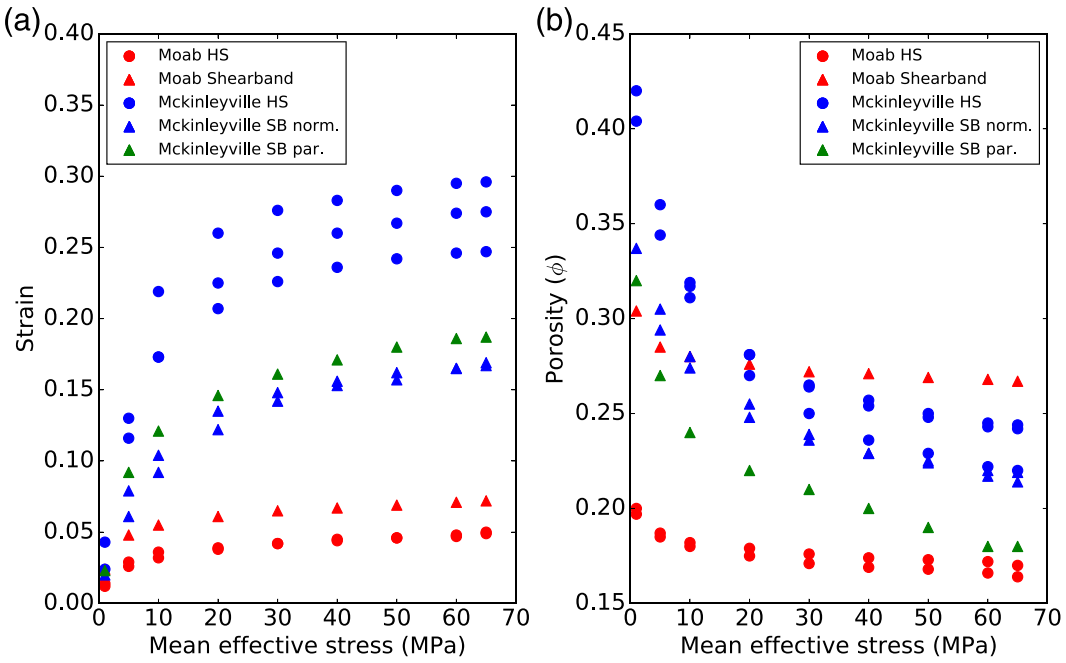

Figure 9. (a) Volumetric strain and (b) porosity (φ) as functions of mean effective stress for the McKinleyville (blue) and Moab (red) host sands (circles) and shear bands (triangles). All tests were conducted perpendicular to shear bands, except for a single test parallel to a shear band from McKinleyville (green triangles).

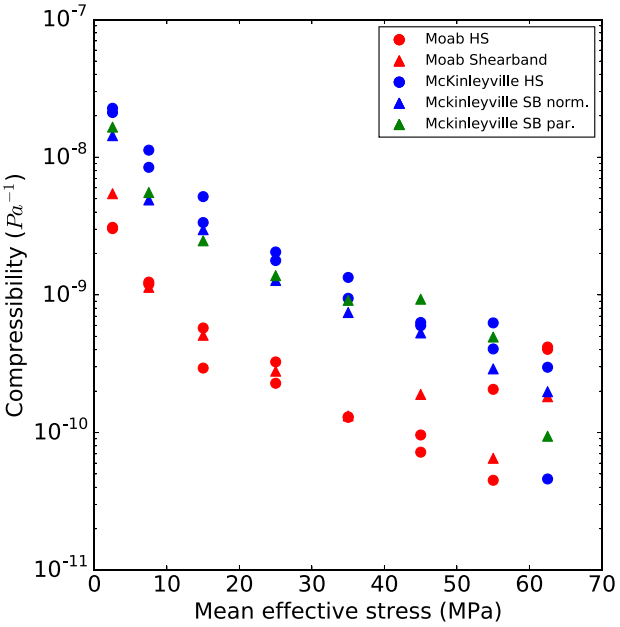

Figure 10. Compressibility as a function of mean effective stresses, for McKinleyville (blue and green) and Moab (red) host sand (circles) and shear bands (triangles).

stresses <5 MPa. Although the majority of measurements were conducted perpendicular to band orientation, we conducted a single experiment to explore possible permeability anisotropy in the McKinleyville shear bands. The permeability measured parallel to the shear bands ranged from 9.0×10^{-18} to 3.0×10^{-17} m^2, which is within the range of values we obtained for permeability normal to the bands.

Similarly, the permeabilities of the host sandstone and the shear band specimens from Moab separate into two groups. The permeability of the host sandstone is 2.0×10^{-14} m^2 at peak stress, while the material containing the shear bands has a permeability of 2.0×10^{-15} m^2. The permeability of the shear bands at peak stress during the experiments falls within the higher bounds of local permeability measurements made by Fossen (2010) on deformation bands in more northern segments of the Moab fault, with values between 10^{-18} and 10^{-15} m^2. Like the samples from McKinleyville, the permeabilities of the deformation bands from Moab are approximately an order of magnitude lower than those for the host material. The rate of permeability decrease with increasing mean effective stress is generally less for the Moab samples than the corresponding the rate of decrease for the McKinleyville samples. The values we report are in good agreement with permeabilities of sandstones and unconsolidated sands over the same porosity range reported by Nelson (1994).

Porosity has a big impact on permeability of sandstone. We find that permeability decreases log-linearly with decreasing porosity (Figure 11b), consistent with data for sandstones and other sedimentary rocks (e.g., David et al., 1994, 2001; Wong & Zhu, 1999). Because porosity decreases with increasing effective stress, the arrow in Figure 11b shows the general decrease in permeability during loading. The samples from McKinleyville and the Moab

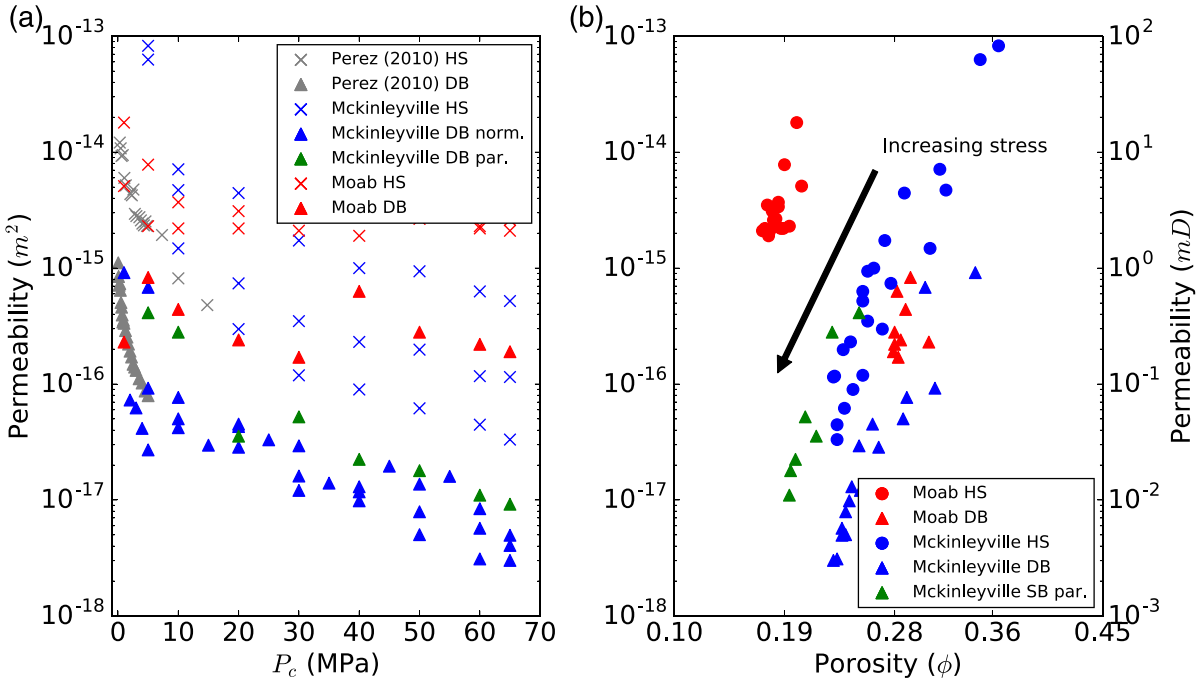

Figure 11. Permeability evolution with mean effective stress (panel a). Permeability is reported in both m^2 and in mD. Previous low stress (<5 MPa) permeability measurements from Perez (2010) are plotted in gray for comparison. Panel (b) shows permeability evolution as a function of porosity.

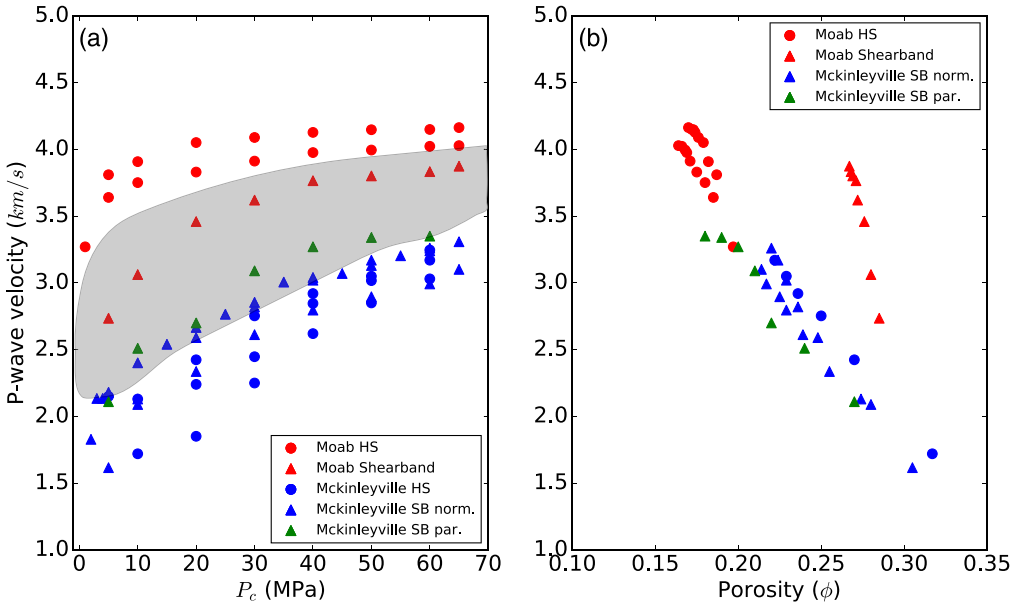

Figure 12. *P* wave velocity as a function of mean effective stress (panel a) and porosity (panel b). Previous *P* wave velocity measurements for sandstones in damage areas surrounding the Moab fault obtained by Flodin et al. (2003) are shown for comparison (gray polygon).

deformation band material follow similar trends of permeability with porosity: permeability decreases from to 9.0×10^{-16} m^2 to 2.0×10^{-18} m^2 as porosity is reduced from 0.35 to 0.23. However, the permeability of Moab host material is ~1 order of magnitude higher than the other materials we tested at a given porosity, with permeability decreasing from 1.0×10^{-14} m^2 to 1.0×10^{-15} m^2 as porosity decreases from 0.19 to 0.16.

4.3. Compressional Wave Speeds

Overall, *P* wave velocity increases with increasing stress and with decreasing porosity, consistent with previous work on sandstones and other sedimentary rocks (e.g., Dvorkin et al., 1999; Erickson & Jarrard, 1998; Flodin et al., 2003). *P* wave velocities for samples from the McKinleyville site range from 1.7–3.2 km/s, whereas the velocities of the Moab samples range from 2.7–4.2 km/s, over effective stresses from 1–65 MPa (Figure 12a).

The McKinleyville shear band material exhibited higher velocities than the host material, with *Vp* ranging from 2.1–3.3 km/s, versus 2.0 to 2.9 km/s for the host sand. However, at a given porosity, the compressional wave velocity was slightly slower (by ~0.1 km/s) in the shear band material compared with the host material (Figure 12b). There is also no clear evidence for anisotropy, although our data are limited to a single experiment (green triangles in Figure 12). In contrast, the shear band material from Moab has lower *Vp* than the host material, with velocities ranging from 2.7 to 3.4 km/s, versus 3.3 to 4.1 km/s for the host material.

4.4. Microstructure and Particle Size Distribution

The host sand from McKinleyville is composed of uniform angular grains, whereas the shear bands contain a wide particle size distribution with phyllosilicates filling the pore space (K. Cashman & S. Cashman, 2000; Kaproth et al., 2010; Perez, 2010) (Figures 6, 7a, and 7b). In contrast, the Moab host sandstone exhibits a wider grain size distribution, with highly angular grains (Figure 7c). The host material adjacent to the Moab shear bands has uniform grain size with little to no phyllosilicate deposition. However, the interior of the shear bands contains a wider distribution of grain sizes, and the pore space is filled with small phyllosilicate grains and cement (Figure 7d).

The Moab host sandstone is grain supported with pervasive cement while the Moab material containing (and adjacent to) shear bands is less strongly cemented, though it is also grain supported (Figures 7d and 8a). In SEM images it appears that the material immediately adjacent to shear bands has higher porosity

than the intact host material and is less extensively cemented, whereas the core of the shear bands is more strongly cemented and has lower porosity.

Unlike the Moab host material and shear bands, the McKinleyville deformation bands are matrix supported. They exhibit a bimodal distribution centered on grain diameters of 190 and 50 μm (Figure 6), which are consistent with measurements made by Kaproth et al. (2010). The McKinleyville shear bands also show a small peak (<0.5%) at a mean grain diameter of 500 nm. Approximately 50% of the total volume of the solid phase of the McKinleyville shear bands consists of grains finer than 100 μm while fine grains (<100 μm) make up only 10% of the total volume of the host sands, similar to results reported by Cashman et al. (2007) and Kaproth et al. (2010). Both the Moab sandstones and shear bands exhibit a consistent, unimodal grain size distribution (Figure 6).

5. Discussion

The petrophysical and mechanical data from our experiments provide insight into the characteristics of two end-member sandstones. The presence of cataclastic deformation bands suggests a dynamic stress environment that has altered the initial structure of the host material and has therefore fundamentally changed its mechanical and petrophysical properties. The expectation is that cataclastic deformation bands will significantly reduce permeability across structures (e.g., Aydin, 2000; Fossen & Hesthammer, 1998; Sample et al., 2006). Likewise, the elastic properties of the material will change with the introduction of localized deformation, and the presence of pervasive cement will control the material's response to loading. The mechanisms that underlie the change in properties include grain comminution, cementation, pore size reduction, grain alignment, and authigenic mineral growth (Ballas et al., 2013; Cresswell & Barton, 2003; Kaproth et al., 2010).

Our compressibility data indicate that the Moab material is approximately an order of magnitude stiffer than that from McKinleyville (Figure 10). We suggest that the elastic properties of these materials are controlled by the distribution and strength of cement. While the SEM images show the presence of cement in both the McKinleyville shear bands and the Moab samples, the cement within the bands from McKinleyville consists of comminuted quartz grains and some authigenic mineral growth (Figure 7). In contrast, the cement in the Moab samples is more pervasive, finer grained, and more structurally integral than the cement in the McKinleyville shear bands. We also observe that porosity converges at high effective stress for deformation bands in poorly cemented sands. This is the result of grain contacts becoming the primary contributor to skeleton rigidity. Conversely, the porosities in well-cemented sandstones do not converge because the cement controls the deformation accommodated by the material skeleton.

At mean effective stresses below 10 MPa, the permeability of samples from both study areas decreases rapidly with increasing mean effective stress. However, the magnitude of decrease following the initial sharp decline is different for samples from McKinleyville and Moab (Figure 11). The permeability of the samples from McKinleyville decreases by 2 orders of magnitude over this initial loading phase, while permeabilities of Moab samples decrease less than 1 order of magnitude over this same stress range, and decrease less throughout the entirety of the experiment. We interpret that this occurs because the Moab material is stiffer, such that increasing the mean effective stress has a smaller impact on the pore structure and pore throat dimension, leading to lower sensitivity of permeability to loading (cf. Figures 9b and 11).

The 2 order of magnitude difference between the permeabilities of McKinleyville host material and its shear bands is attributed to the presence of cement and increased fine particle abundance within the shear band core (K. Cashman & S. Cashman, 2000; Kaproth et al., 2010; Perez, 2010). This hypothesis is consistent with the lower porosity within the shear bands relative to the host sand, and the increased fine particle abundance in the shear bands (Figure 6). This can be explained by comminution in the shear bands (Figure 13, top), coupled with the growth of phyllosilicates, facilitated by the increased surface area of grains and breakdown of lithic clasts containing feldspars and clays (Lommatzsch et al., 2015).

The permeability of the Moab shear bands, like the McKinleyville shear bands, is lower than the surrounding host material (Figures 8a, 11, and 13, bottom row). However, in contrast to the McKinleyville shear bands and host sand, the Moab material exhibits little sensitivity to increasing effective stress. The combination of lower compressibility and a higher degree of cementation in the host sands relative to the

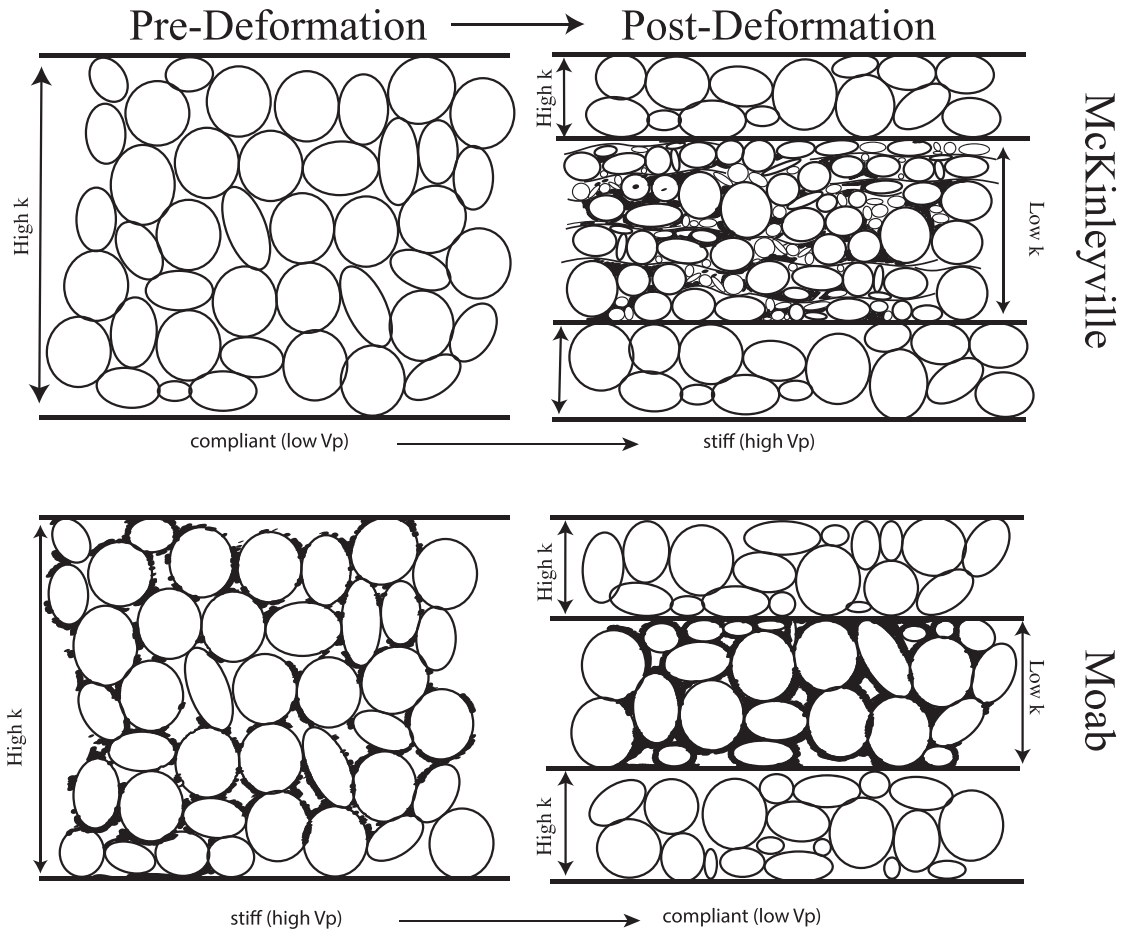

Figure 13. Schematic diagram illustrating the mechanisms we interpret to control differences in permeability and stiffness between host sand (stone) and deformation bands. For unconsolidated sandstone, the development of deformation bands creates layers of dense material adjacent to unchanged material (top panels). In contrast, the formation of deformation bands in overconsolidated sandstone disrupts and damages the adjacent material, weakening the overall structure (bottom panels).

McKinleyville material suggests that the porosity and permeability trends seen during loading are related to microcrack closure and modest compression of the pore spaces (Figures 7c and 7d). Although the bulk porosity of samples from Moab is higher in the material containing the shear bands, the permeability reduction within the shear bands dominates the fluid flow properties of the aggregate material, thereby lowering the overall permeability (Figure 13). We expect that permeabilities of the shear bands (computed from Equation 5) represent an upper bound and could be lower if the matrix permeability is higher than we assumed. The shear bands from the Moab locality are cemented, appear to have very low porosity, and exhibit a broader grain size distribution than the host sandstone (Figure 6). We interpret that the permeability reduction is caused by these three effects acting in concert, resulting from grain reorientation and breakage during shear localization combined with cementation and the growth of authigenic clays (Fisher & Knipe, 2001; Perez, 2010). While we cannot rule out the potential role of shear- or deformation-enhanced grain alignment in the bands in both permeability and porosity reduction relative to the host material (e.g., Fossen et al., 2007; Kaproth et al., 2010), we observe little evidence for this in SEM images; this interpretation is also consistent with both the small shear strains experienced by the bands we studied, and the overall low phyllosilicate abundance.

P wave velocities exhibit a sharp increase with the initial application of mean effective stress (100 kPa to 10 MPa) for all samples, and a subsequent gradual increase to a maximum value at ~65 MPa mean effective stress (Figure 12a), mimicking the trends in compressibility. The *P* wave velocities for the Moab samples are consistently higher than the samples from McKinleyville, likely due to the presence of cement (Dvorkin &

Nur, 1996; Flodin et al., 2003). Interestingly, the shear bands and host material from McKinleyville exhibit very similar *P* wave velocities at stresses >10 MPa. Although cement enhances grain contacts (Dvorkin & Nur, 1996), microcracks or damaged cement tend to reduce the *P* wave velocity with respect to the host material.

In contrast to the McKinleyville samples, *P* wave velocity is lower in the Moab shear bands compared to the host material. Taken together with our SEM observations of increased porosity and disrupted cement adjacent to the shear bands (Figure 10d), suggests that shear band formation and architecture are fundamentally different in unconsolidated sands and cemented or overconsolidated sandstones (e.g., Caine et al., 1996) (Figure 13). In the cemented case, shear band formation leads to damage and disruption of grain contacts or cement in the brittle host material surrounding the bands, leading to reduced elastic moduli and hence a reduction in *P* wave velocity. This behavior is absent within the McKinleyville samples because shear bands in these unconsolidated sands form by comminution, grain repacking, and minor phyllosilicate growth, while the adjacent host material remains essentially unmodified. As a result, the shear bands represent simpler, localized structures where elastic moduli and *Vp* are increased and grain size and permeability are reduced, within an otherwise intact host material. In this case, the dominant effect of shear band formation is the local reduction in grain size and porosity.

6. Conclusions

Shear bands are common features in porous sandstones. We show that their permeability, compressibility, porosity, and elastic wave speed evolve systematically when subjected to changing effective stress, for example, as would occur during burial or as a result of fluid extraction or injection. Our results also indicate that the change of these physical properties during loading depends on both the cementation state of the host material and the nature of the shear bands. We find that permeability decreases systematically in shear bands relative to their host material. We also find that *P* wave velocity increases in shear bands formed in unconsolidated sands, but decreases in those that are formed in cemented or lithified sandstones. We attribute this difference to distinct differences in shear band architecture for the two types of host material.

Our data suggest that shear deformation should lead to a marked decrease in bulk permeability for both the unconsolidated and lithified end-members, and thus the formation and presence of deformation bands should reduce aquifer or reservoir permeability and lead to potential compartmentalization. This effect will become accentuated with increasing effective stress, as might occur during depletion or overpumping. Grain comminution and cement deposition are the primary processes controlling permeability decrease within the shear bands. In addition, our observations suggest that in general, the mechanical strength of overconsolidated sandstones is reduced when deformation bands are formed due to the disruption of cement in the regions around the bands. In contrast, deformation band formation in poorly consolidated sands increases the elastic moduli by reducing porosity and stiffening the matrix. In both cases, the bands themselves act as barriers to fluid flow, which create channels of higher permeability material sandwiched between low permeability bands. Further work is necessary to characterize the mineralogical composition of the deformation band cement to determine the abundance of phyllosilicates, which contribute to permeability reduction (Perez, 2010) and to quantify the conditions of formation and controls on spacing of shear bands.

Data Availability Statement

Data generated for this manuscript are freely available from this site (https://doi.org/10.18738/T8/BECJYG).

Acknowledgments
We thank S. Swavley for technical support for laboratory measurements. This research was supported by NSF-EAR Award 1215856 to Demian Saffer and Chris Marone NSF-EAR award 1520760, DE-EE0006762, and a GDL Foundation Fellowship to Peter Miller.

References

Antonellini, M. A., Aydin, A., & Pollard, D. D. (1994). Microstructure of deformation bands in porous sandstone, arches National Park, UT. *Journal of Structural Geology*, *16*(7), 941–959. https://doi.org/10.1016/0191-8141(94)90077-9

Aydin, A. (1978). Small faults formed as deformation bands in sandstone. *Pure and Applied Geophysics PAGEOPH*, *116*(4–5), 913–930. https://doi.org/10.1007/BF00876546

Aydin, A. (2000). Fractures, faults, and hydrocarbon entrapment, migration and flow. *Marine and Petroleum Geology*, *17*(7), 797–814. https://doi.org/10.1016/S0264-8172(00)00020-9

Aydin, A., & Johnson, A. M. (1983). Analysis of faulting in porous sandstones. *Journal of Structural Geology*, *5*(1), 19–31. https://doi.org/10.1016/0191-8141(83)90004-4

Ballas, G., Soliva, R., Sizun, J. P., Fossen, H., Benedicto, A., & Skurtveit, E. (2013). Shear-enhanced compaction bands formed at shallow burial conditions; implications for fluid flow (Provence, France). *Journal of Structural Geology*, *47*, 3–15. https://doi.org/10.1016/j.jsg.2012.11.008

Berg, S. S., & Skar, T. (2005). Controls on damage zone asymmetry of a normal fault zone: Outcrop analyses of a segment of the Moab fault, SE Utah. *Journal of Structural Geology*, *27*(10), 1803–1822. https://doi.org/10.1016/j.jsg.2005.04.012

Brzesowsky, R. H., Spiers, C. J., Peach, C. J., & Hangx, S. J. T. (2014). Time-independent compaction behavior of quartz sands. *Journal of Geophysical Research: Solid Earth*, *119*, 936–956. https://doi.org/10.1002/2013JB010444

Caine, J. S., Evans, J. P., & Forster, C. B. (1996). Fault zone architecture and permeability structure. *Geology*, *24*(11), 1025–1028. https://doi.org/10.1130/0091-7613(1996)024<1025:FZAAPS>2.3.CO;2

Carpenter, B. M., Kitajima, H., Sutherland, R., Townend, J., Toy, V. G., & Saffer, D. M. (2014). Hydraulic and acoustic properties of the active Alpine Fault, New Zealand: Laboratory measurements on DFDP-1 drill core. *Earth and Planetary Science Letters*, *390*, 45–51. https://doi.org/10.1016/j.epsl.2013.12.023

Cashman, S., & Cashman, K. (2000). Cataclasis and deformation-band formation in unconsolidated marine terrace sand, Humboldt County, California. *Geology*, *28*(2), 111–114. https://doi.org/10.1130/0091-7613(2000)28<111:CADFIU>2.0.CO;2

Cashman, S. M., Baldwin, J. N., Cashman, K. V., Swanson, K., & Crawford, R. (2007). Microstructures developed by coseismic and aseismic faulting in near-surface sediments, San Andres fault, California. *Geology*, *35*(7), 611–614. https://doi.org/10.1130/G23545A.1

Cresswell, A. W., & Barton, M. E. (2003). Direct shear tests on an uncemented, and a very slightly cemented, locked sand. *Quarterly Journal of Engineering Geology and Hydrogeology*, *36*(2), 119–132.

Davatzes, N. C., Eichhubl, P., & Aydin, A. (2005). Structural evolution of fault zones in sandstone by multiple deformation mechanisms: Moab fault, Southeast Utah. *Bulletin of the Geological Society of America*, *117*(1), 135–148. https://doi.org/10.1130/B25473.1

David, C., Menendez, B., Zhu, W., & Wong, T. F. (2001). Mechanical compaction, microstructures and permeability evolution in sandstones. *Physics and Chemistry of the Earth, Part A: Solid Earth and Geodesy*, *26*(1–2), 45–51. https://doi.org/10.1016/S1464-1895(01)00021-7

David, C., Wong, T. F., Zhu, W., & Zhang, J. (1994). Laboratory measurement of compaction-induced permeability change in porous rocks: Implications for the generation and maintenance of pore pressure excess in the crust. *Pure and Applied Geophysics PAGEOPH*, *143*(1–3), 425–456. https://doi.org/10.1007/BF00874337

Doelling, H. H. (2001). Geologic map of the Moab and eastern part of the San Rafael Desert 30′ × 60′ quadrangles, Grand and Emery Counties, Utah, and Mesa County, Colorado. Utah Geological Survey.

Dvorkin, J., & Nur, A. (1996). Elasticity of high-porosity sandstones: Theory for two North Sea data sets. *Geophysics*, *61*(5), 1363–1370. https://doi.org/10.1190/1.1444059

Dvorkin, J., Prasad, M., Sakai, A., & Lavoie, D. (1999). Elasticity of marine sediments: Rock physics modeling. *Geophysical Research Letters*, *26*(12), 1781–1784. https://doi.org/10.1029/1999GL900332

Erickson, N., & Jarrard, R. D. (1998). Velocity-porosity relationships for water-saturated sediments. *Journal of Geophysical Research*, *103*(B12), 30,385–30,406. https://doi.org/10.1029/98JB02128

Fetter, C. W. (2001). *Applied hydrogeology* (Fourth ed.). Upper Saddle River, New Jersey: Prentice Hall.

Fisher, Q. J., & Knipe, R. J. (2001). The permeability of faults within siliciclastic petroleum reservoirs of the North Sea and Norwegian continental shelf. *Marine and Petroleum Geology*, *18*(10), 1063–1081. https://doi.org/10.1016/S0264-8172(01)00042-3

Flodin, E., Prasad, M., & Aydin, A. (2003). Petrophysical constraints on deformation styles in Aztec sandstone, southern Nevada, USA. *Pure and Applied Geophysics*, *160*(9), 1589–1610. https://doi.org/10.1007/s00024-003-2377-1

Fossen, H. (2010). Deformation bands formed during soft-sediment deformation: Observations from SE Utah. *Marine and Petroleum Geology*, *27*(1), 215–222. https://doi.org/10.1016/j.marpetgeo.2009.06.005

Fossen, H., & Hesthammer, J. (1998). Deformation bands and their significance in porous sandstone reservoirs. *First Break*, *16*(1), 21–25. https://doi.org/10.1046/j.1365-2397.1998.00683.x

Fossen, H., Schultz, R., Shipton, Z. K., & Mair, K. (2007). Deformation bands in sandstone: a review. *Journal of the Geological Society, London*, *164*(4), 755–769. https://doi.org/10.1144/0016-76492006-036

Hashimoto, Y., Tobin, H. J., & Knuth, M. (2010). Velocity-porosity relationships for slope apron and accreted sediments in the Nankai Trough Seismogenic Zone Experiment, Integrated Ocean Drilling Program Expedition 315 Site C0001. *Geochemistry, Geophysics, Geosystems*, *11*, Q0AD05. https://doi.org/10.1029/2010GC003217

Heap, M. J., Brantut, N., Baud, P., & Meredith, P. G. (2015). Time-dependent compaction band formation in sandstone. *Journal of Geophysical Research: Solid Earth*, *120* (accepted, 1–20).

Heiland, J., & Raab, S. (2001). Experimental investigation of the influence of differential stress permeability of a lower permian (Rotliegend) sandstone deformed in the brittle deformation field. *Physics and Chemistry of the Earth, Part A: Solid Earth and Geodesy*, *26*(1–2), 33–38. https://doi.org/10.1016/S1464-1895(01)00019-9

Kaproth, B. M., Cashman, S. M., & Marone, C. (2010). Deformation band formation and strength evolution in unlithified sand: The role of grain breakage. *Journal of Geophysical Research: Solid Earth*, *115*, 1–11. https://doi.org/10.1029/2010jb007406

Karig, D. E., & Ask, M. V. S. (2003). Geological perspectives on consolidation of clay rich marine sediments. *Journal of Geophysical Research*, *108*(B4), 2197. https://doi.org/10.1029/2001jb000652

Karig, D. E., & Hou, G. (1992). High-stress consolidation experiments and their geologic implications. *Journal of Geophysical Research*, *97*(B1), 289–300. https://doi.org/10.1029/91JB02247

Kelsey, H. M., & Carver, G. A. (1988). Late Neogene and quaternary tectonics associated with northward growth of the San Andreas transform fault, northern California. *Journal of Geophysical Research*, *93*(B5), 4797–4819. https://doi.org/10.1029/JB093iB05p04797

Kenigsberg, A. R., Rivière, J., Marone, C., & Saffer, D. M. (2020). A method for determining absolute ultrasonic velocities and elastic properties of experimental shear zones. *International Journal of Rock Mechanics and Mining Sciences*, *130*, 104306. https://doi.org/10.1016/j.ijrmms.2020.104306

Knuth, M. W., Tobin, H. J., & Marone, C. (2013). Evolution of ultrasonic velocity and dynamic elastic moduli with shear strain in granular layers. *Granular Matter*, *15*, 499–515. https://doi.org/10.1007/s10035-013-0420-1

Konert, M., & Vandenberghe, J. (1997). Comparison of laser grain size analysis with pipette and sieve analysis: a solution for the underestimation of the clay fraction. *Sedimentology*, *44*(3), 523–535. https://doi.org/10.1046/j.1365-3091.1997.d01-38.x

Lommatzsch, M., Exner, U., Gier, S., & Grasemann, B. (2015). Structural and chemical controls of deformation bands on fluid flow: Interplay between cataclasis and diagenetic alteration. *AAPG Bulletin*, *99*, 689–710. https://doi.org/10.1306/10081413162

Nelson, P. (1994). Permeability-porosity relationships in sedimentary rocks. *The Log Analyst*, *35*(4), 38–62.

Perez, E. G. (2010). Laboratory measurements of permeability reduction in naturally occurring shear bands formed in unlithified sand. (Master's thesis). Penn State University. State college, PA

Prasad, M. (2002). Acoustic measurements in unconsolidated sands at low effective pressure and overpressure detection. *Geophysics*, *67*(2), 405–412. https://doi.org/10.1190/1.1468600

Rawling, G. C., & Goodwin, L. B. (2003). Cataclasis and particulate flow in faulted, poorly lithified sediments. *Journal of Structural Geology*, *25*(3), 317–331. https://doi.org/10.1016/S0191-8141(02)00041-X

Rotevatn, A., Sandve, T. H., Keilegavlen, E., Kolyukhin, D., & Fossen, H. (2013). Deformation bands and their impact on fluid flow in sandstone reservoirs of natural thickness variations. *Geofluids*, *13*, p1–p13. https://doi.org/10.1111/gfl.12030

Sample, J. C., Woods, S., Bender, E., & Loveall, M. (2006). Relationship between deformation bands and petroleum migration in an exhumed reservoir rock, Los Angeles Basin, California, USA. *Geofluids*, *6*(2), 105–112. https://doi.org/10.1111/j.1468-8123.2005.00131.x

Schultz, R. a., & Siddharthan, R. (2005). A general framework for the occurrence and faulting of deformation bands in porous granular rocks. *Tectonophysics*, *411*(1–4), 1–18. https://doi.org/10.1016/j.tecto.2005.07.008

Skurtveit, E., Torabi, A., Gabrielsen, R. H., & Zoback, M. D. (2013). Experimental Investigation of deformation mechanisms during shear enhanced compaction in poorly lithified sandstone and sand. *JGR: Solid Earth*, *118*, 4083–4100. https://doi.org/10.1002/jgrb.50342

Storti, F., & Balsamo, F. (2010). Particle size distributions by laser diffraction: Sensitivity of granular matter strength to analytical operating procedures. *Solid Earth*, *1*(1), 25–48. https://doi.org/10.5194/se-1-25-2010

Wang, J. a., & Park, H. D. (2002). Fluid permeability of sedimentary rocks in a complete stress-strain process. *Engineering Geology*, *63*(3–4), 291–300. https://doi.org/10.1016/S0013-7952(01)00088-6

Wong, T., David, C., & Zhu, W. (1997). The transition from brittle faulting to cataclastic flow in porous sandstones: Mechanical deformation. *Journal of Geophysical Research*, *102*(B2), 3009–3025. https://doi.org/10.1029/96JB03281

Wong, T., Szeto, H., & Zhang, J. (2015). Effect of loading path and porosity on the failure mode of porous rocks. *Applied Mechanics Reviews*, *45*, 281–293.

Wong, T., & Zhu, W. (1999). Brittle faulting and permeability evolution: Hydromechanical measurement, microstructural observation, and network modeling. *Geophysical Monograph by The American Geophysical Union*, *113*, 83–99. https://doi.org/10.1029/gm113p0083